# Diverse Slot-Opening Designs for Cogging Torque and Performance Optimization in PM Machines

Litao Dai, *Member*, *IEEE*, Shuangxia Niu, *Senior Member*, *IEEE*, Jian Gao, Kun Liu, Shoudao Huang, *Senior Member*, *IEEE*, and W. L. Chan, *Senior Member*, *IEEE*

***Abstract*—The slot-opening structure in permanent magnet (PM) machines plays a crucial role in optimizing torque, electromotive force, and electromagnetic vibration metrics. Consequently, significant attention has been devoted to optimizing its design, particularly focused on reducing cogging torque through methods such as tooth shape optimization and dummy slots. However, current slot-opening design techniques face challenges, particularly in compromising average torque and inadequately suppressing cogging torque due to simplistic modifications of slot reluctance harmonics. In contrast, this study introduces a comprehensive slot harmonics configuration method alongside diverse slot-opening design schemes, showcasing enhanced effectiveness in mitigating cogging torque in various PM machine structures with different pole-slot combinations. The key of this approach involves adjusting the airgap magnetic reluctance harmonics to amplify the least common multiple of interacting harmonics responsible for cogging torque generation. Through extensive validation via finite-element method and experimental test, the proposed method emerges as a promising solution for effectively reducing cogging torque and enhancing the overall performance of PM machines.**

***Index Terms*—Permanent magnet machines, torque, design methodology, cogging torque.**

## I. INTRODUCTION

In recent years, permanent magnet machines (PMMs) have found extensive applications in various fields such as electrified transportation [1], [2], industrial sector [3], and household appliances [4] owing to their notable advantages of high efficiency and power density. However, a notable drawback of PMMs is the presence of inherent cogging torque [5], which manifests periodically and significantly, impacting torque performance, particularly under low-load conditions. Consequently, cogging torque suppression has emerged as a focal point in the realm of motor drives [6], [7].

Cogging torque in PMMs arises from the relative motion between a motor side generating magnetic flux and another side exhibiting uneven magnetic reluctance. Based on this principle, methods for reducing cogging torque can be distinctly categorized into two main groups:

1. Design optimization for the flux side

Flux side optimization primarily targets the side containing PMs responsible for flux generation. This optimization pertains to the rotor side of PM synchronous machines (PMSMs) [8], [9], [10], [11], [12], [13], PM synchronous reluctance machines [14], consequent pole PM machines [15], as well as the stator side corresponding to flux-switching PM machines [16], [17] and PM vernier machines [18]. These studies employ different techniques such as optimizing PM shapes [12], [13], [17], refining the core surface near the airgap [8], [10], [11], [14], [15], constructing asymmetrical magnetic poles [9], and optimizing the flux bridge shape [16] to modulate the generated PM flux and reduce cogging torque.

2. Design optimization for the reluctance side

Reluctance side optimization involves modifying the reluctance harmonics characterized by uneven magnetic reluctance around the airgap periphery. This optimization strategy includes shaping the stator teeth of PMSMs [19] and brushless dc machines [20], as well as by shaping the rotor teeth in flux-switching PM machines [21], [22], and PM homopolar inductor machines [23]. Researchers have effectively reduced cogging torque by adjusting the amplitude of reluctance side harmonics through slot-opening structure modifications. Another method of modifying reluctance side harmonics is by integrating dummy slots in the teeth, which can influence either the fundamental slot harmonics [24], [25], [26] or higher-order slot harmonics [21], [27].

In summary, both optimization paths for the flux side and reluctance side target specific harmonics that contribute to cogging torque—whether they are flux or reluctance-related. Given the potential impact of flux harmonics on various motor performances like electromotive force (EMF) distortion and reduced torque output, minimizing cogging torque without compromising crucial motor aspects poses a significant challenge. To tackle this complexity, employing multi-objective design optimization with stochastic algorithm is recommended [28]. However, fine-tuning and optimizing flux harmonics prove to be a more complicated task.

On the other hand, reluctance side optimization methods offer simpler implementation and may have fewer compromises on motor performance. However, current methods for optimizing reluctance harmonics exhibit limited effectiveness. Specifically, adjusting slot-opening parameters has a modest effect on reluctance slot harmonics, and the addition of multiple

Litao Dai, Shuangxia Niu, and W. L. Chan are with the Hong Kong Polytechnic University, Hong Kong, 999077, China (email: litao.dai@polyu.edu.hk; eesxniu@polyu.edu.hk; wai-lok.chan@polyu.edu.hk). (*Corresponding author: Shuangxia Niu.*)

Jian Gao, Kun Liu, and Shoudao Huang are with the Hunan University, Changsha, 410082, China (email: gaojian0895@hnu.edu.cn; kunliu@hnu.edu.cn; hsd1962@hnu.edu.cn).

dummy slots expands the effective airgap volume, leading to reduced flux density and torque output. Hence, there is great potential in exploring reluctance harmonic optimization for mitigating cogging torque.

To develop a more efficient path for cogging torque reduction and to fully leverage the minimal impact of reluctance side harmonics on overall motor performance, this paper presents a novel and comprehensive approach for configuring reluctance side harmonics, alongside diverse slot harmonics configuration (SHC) schemes. When compared to existing slot opening design methods, certain limitations can be identified, including: 1) Ineffective reduction of cogging torque, exemplified by methods like tooth profile modification [19], [20]. 2) Challenges in achieving comprehensive adaptability for different pole-slot combinations while ensuring that other critical performance aspects are not compromised, illustrated by methods such as asymmetrically sized tooth design [29] and non-uniformly distributed slot opening design [30], [31], [32]. 3) Compromises in average torque when employing conventional dummy slot construction methods [24], [26], [33].

The proposed method introduces several innovations and contributions:

(1) The introduction of SHC coefficients enables the creation of diverse stator design schemes to optimize machine performance.
(2) By utilizing the cogging torque mechanism, a design principle is proposed to maximize the least common multiple (LCM) between the number of slots (including dummy slots) and the number of poles, effectively reducing cogging torque and mitigating adverse effects.
(3) A comprehensive study was conducted to analyze the impact of different SHC coefficients across various pole-slot combinations on motor performance, leading to specific design guidelines.

The proposed approach offers the following advantages:

(1) The method effectively suppresses cogging torque and optimizes motor performance, with straightforward implementation and minimal cost increase.
(2) It is broadly applicable to both fractional and integer slot configurations and various rotor PM structures.
(3) It holds research potential in other PM machine topologies, including salient pole machines, linear machines, and axial flux machines.

This paper is structured as follows: Section II explores the relationship between cogging torque and field harmonics. Section III provides a detailed presentation of the proposed method. In Section IV, multiple case studies involving different motor structures are conducted. Section V focuses on experimental verification. Finally, conclusions are drawn.

## II. Harmonic Model of Cogging Torque

In this section, the general manifestations of rotor magnetomotive force (MMF) and airgap reluctance harmonics, as well as the outcomes of their interactions, are elucidated.

### A. Harmonic Model of Cogging Torque

Based on the energy method, the cogging torque in motion can be solved by:

$$T_{cog} = -\frac{\partial W_{mag.cog}}{\partial t} \tag{1}$$

where $W_{mag.cog}$ represents the magnetic energy stored in the airgap, $t$ denotes the running time.

During motor operation, $W_{mag.cog}$ can be expressed as:

$$W_{mag.cog} = \int \frac{B_r(\theta_m,t)^2}{2\mu_0} dV_{\mathrm{ag}} \tag{2}$$

where $V_{\mathrm{ag}}$ is the airgap volume; $\mu_0$ is the vacuum permeability; $B_r(\theta_m,t)$ is the airgap flux density, which can be expressed as a function of the spatial angle ($\theta_m$) and time, as shown below:

$$B_r(\theta_m,t) = \frac{F_r(\theta_m,t)\Lambda_S(\theta_m)}{S_{\mathrm{ag}}} \tag{3}$$

where $S_{\mathrm{ag}}$ is the area of airgap. $F_r(\theta_m,t)$ represents the rotor MMF, and $\Lambda_S(\theta_m)$ represents the magnetic conductance along the airgap circumference.

Furthermore, the rotor MMF is expressed as a general Fourier series form, as shown in:

$$F_r(\theta_m,t) = \sum_{\nu_r=1,3,5,\dots} (-1)^{\frac{\nu_r-1}{2}} A_{Fr}(\nu_r)\cos\left(\nu_r p_N(\theta_m - \omega_m t)\right) \tag{4}$$

where $\nu_r$ represents the order of rotor MMF harmonic; $A_{Fr}(\nu_r)$ is the amplitude of the $\nu_r$-th MMF harmonic; $p_N$ is the number of pole-pairs; $\omega_m$ is the rotational speed of rotor.

The airgap magnetic conductance with slotting effect, $\Lambda_S(\theta_m)$, can be expressed in the form of Fourier series, as shown below:

$$\Lambda_S(\theta_m) = \sum_{\nu_Z=0,1,2,\dots} \Lambda_{As}(\nu_Z)\cos(\nu_Z Z_1 \theta_m) \tag{5}$$

where $Z_1$ is the number of slots; $\nu_Z$ is the order of the slot harmonics ($\nu_Z = 0,1,2,\dots$); $\Lambda_{AS}(\nu_Z)$ is the amplitude of the $\nu_Z$-th slot harmonic.

By substituting (3), (4), and (5) into (2), the general expression for $W_{mag.cog}$ can be obtained, as follows:

$$\begin{aligned}
W_{mag.cog}(\theta_m,t) = {} & \frac{(R_{S0}^2 - R_{r1}^2)L_1}{32\mu_0} \sum_{\nu_{r1}}\sum_{\nu_{r2}}\sum_{\nu_{Z1}}\sum_{\nu_{Z2}} \Big\{ \\
& (-1)^{\frac{\nu_{r1}+\nu_{r2}}{2}-1} A_{Fr}(\nu_{r1})A_{Fr}(\nu_{r2})\Lambda_{As}(\nu_{Z1})\Lambda_{As}(\nu_{Z2}) \Big[ \\
& \cos\left((\nu_{r1}+\nu_{r2})\omega_e t - \left((\nu_{r1}+\nu_{r2})p_N + (\nu_{Z1}+\nu_{Z2})Z_1\right)\theta_m\right) + \\
& \cos\left((\nu_{r1}+\nu_{r2})\omega_e t - \left((\nu_{r1}+\nu_{r2})p_N + (\nu_{Z1}-\nu_{Z2})Z_1\right)\theta_m\right) + \\
& \cos\left((\nu_{r1}+\nu_{r2})\omega_e t - \left((\nu_{r1}+\nu_{r2})p_N - (\nu_{Z1}+\nu_{Z2})Z_1\right)\theta_m\right) + \\
& \cos\left((\nu_{r1}+\nu_{r2})\omega_e t - \left((\nu_{r1}+\nu_{r2})p_N - (\nu_{Z1}-\nu_{Z2})Z_1\right)\theta_m\right) + \\
& \cos\left((\nu_{r1}-\nu_{r2})\omega_e t - \left((\nu_{r1}-\nu_{r2})p_N + (\nu_{Z1}+\nu_{Z2})Z_1\right)\theta_m\right) + \\
& \cos\left((\nu_{r1}-\nu_{r2})\omega_e t - \left((\nu_{r1}-\nu_{r2})p_N + (\nu_{Z1}-\nu_{Z2})Z_1\right)\theta_m\right) + \\
& \cos\left((\nu_{r1}-\nu_{r2})\omega_e t - \left((\nu_{r1}-\nu_{r2})p_N - (\nu_{Z1}+\nu_{Z2})Z_1\right)\theta_m\right) + \\
& \cos\left((\nu_{r1}-\nu_{r2})\omega_e t - \left((\nu_{r1}-\nu_{r2})p_N - (\nu_{Z1}-\nu_{Z2})Z_1\right)\theta_m\right) \Big] \Big\}
\end{aligned} \tag{6}$$

where $R_{S0}$, $R_{r1}$, $L_1$ represent the stator bore radius, rotor outer radius, and motor length, respectively. $\omega_e$ denotes the electrical speed defined as $\omega_e = p_N\omega_m$.

From (6), it can be observed that the integral of airgap energy is non-zero only when the following conditions are satisfied:

$$\left(\nu_{r1} \pm \nu_{r2}\right) p_N \pm \left(\nu_{Z1} \pm \nu_{Z2}\right) Z_1 = 0 \tag{7}$$

Under the above conditions, the cogging torque can be obtained by substituting (6) into (1) and simplifying it as follows:

$$\begin{aligned} T_{cog} = & \frac{(R_{S0}^2 - R_{r1}^2) L_1 \pi}{16 \mu_0} \sum_{\nu_{r1}} \sum_{\nu_{r2}} \sum_{\nu_{Z1}} \sum_{\nu_{Z2}} \{(-1)^{\frac{\nu_{r1}+\nu_{r2}}{2}-1} \\ & \omega_{CT} A_{Fr}(\nu_{r1}) A_{Fr}(\nu_{r2}) \Lambda_{As}(\nu_{Z1}) \Lambda_{As}(\nu_{Z2}) \sin(\omega_{CT} t)\} \end{aligned} \tag{8}$$

where $\omega_{CT}$ represents the variation speed of the cogging torque and must satisfy the following constraints:

$$\omega_{CT} \in \mathrm{CM}\left((\nu_{r1} \pm \nu_{r2}) p_N, \quad (\nu_{Z1} \pm \nu_{Z2}) Z_1\right) \cdot \omega_m \tag{9}$$

where CM denotes the function of the common multiple.

### *B. Verification for the Cogging Torque Harmonic Model*

To validate the effectiveness of the proposed cogging torque model, an 8-pole 24-slot interior-PMSM is simulated. The motor structure and variable parameters are shown in Fig. 1(a). Initially, the motor possesses the following specifications: a motor diameter of 150 mm, motor length of 60 mm, stator bore diameter of 90 mm, airgap thickness of 1 mm, tooth tip height of 2 mm, PM and its cavity thickness of 3 mm. Additionally, the slot opening ratio ($k_{SO}$) is set at 0.4, representing the ratio of opening width to slot width, while the PM web ratio ($k_{Wb}$) is 0.15, indicating the web width to the maximum available width.

As discussed in Section II.A, the harmonic components of the rotor MMF and airgap magnetic conductance are crucial for accurately computing cogging torque. To acquire this data, the static magnetic field of the model is solved using the finite element method (FEM), enabling derivation of the rotor MMF and airgap conductance harmonics. By integrating the frequency constraints outlined in (9) and the torque totalization in (8), the final cogging torque can be determined. The cogging torque waveform obtained through the proposed method are compared with its from transient-field FEM in Fig. 1(b). The comparison clearly demonstrates that the proposed harmonic model accurately predicts the cogging torque behavior.

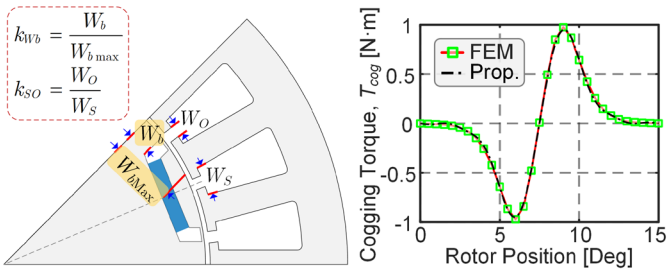


(a) (b)

**Fig. 1.** Verification motor structure and comparative results. (a) Motor structure and parameters illustration. (b) Cogging torque waveform comparison.

Furthermore, to validate the model's accuracy in capturing variations in rotor MMF and airgap conductance harmonics, two parameters can directly influence these harmonics:

(1) PM web ratio $k_{Wb}$, it can adjust rotor MMF harmonics, ranging from 0.05 to 0.5 with a step size of 0.05.

(2) Slot opening ratio $k_{SO}$, it can adjust reluctance harmonics, ranging from 0.05 to 0.5 with a step size of 0.05.

The cogging torque is computed using both methods, and their peak values vary with the variables $k_{Wb}$ and $k_{SO}$ are shown in Fig. 2. The results exhibit a robust agreement between the two methods. This suggests that the developed model can serve as a theoretical foundation for understanding the relationship between field harmonics and cogging torque.

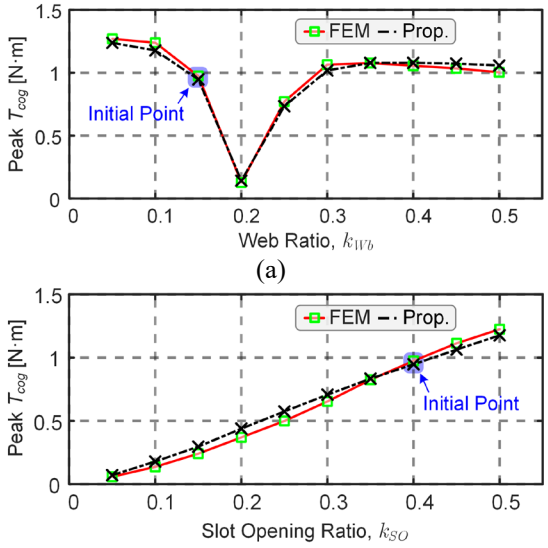


(a)

(b)

**Fig. 2.** Peak cogging torque under parametric scanning. (a) Versus web ratio. (b) Versus slot opening ratio.

### *C. Inferences From the Harmonic Model*

Based on the cogging torque harmonic model, the following important inferences can be derived:

1) **Inference-I**: The generation of cogging torque requires the combined effects of rotor flux harmonics and reluctance slot harmonics. Therefore, adjusting either the reluctance slot harmonics or rotor flux harmonics can effectively suppress cogging torque. These adjustments in harmonic amplitudes can be achieved through structural modifications on the flux side, like optimizing the PM layer, and on the reluctance side, such as altering slot opening width and refining tooth shapes. However, accurately crafting specific desired harmonics poses a challenge.

2) **Inference-II**: Given a fixed number of poles, the combination of rotor MMF harmonics contributing to cogging torque is determined by the number of slots. For instance, in an 8-pole 24-slot motor, the rotor MMF harmonics that largely affect cogging torque are of orders 5 and 7, while in an 8-pole 48-slot motor, they are of orders 11 and 13. It is observed that a larger LCM of the number of slots and poles leads to the involvement of higher-order rotor MMF harmonics in generating cogging torque. These higher-order rotor MMF harmonics exhibit reduced amplitudes, indicating reduced cogging torque. This is particularly evident in practical applications, where fractional-slot PM machines exhibit lower cogging torques

compared to integer-slot machines, especially when the number of slots is close to the number of poles.

## III. Proposed Diverse SHC Method

### A. Implementation of SHC

Fig. 3 presents a comprehensive display of diverse SHC schemes proposed for three-phase PM machines, employing the integration of dummy slots.

In contrast to conventional approach that typically employ whole multiples of the actual slot count (e.g., 2 times or 3 times), the proposed method introduces a fractional ratio of dummy slots to actual slots, represented by the coefficient $r_{\mathrm{FD}}$. It is worth noting that all slots and openings on the stator are uniformly distributed and of the same size. The distinction between real slots and dummy slots depends on whether they are located below the slots or the teeth.

The expected airgap conductance after applying the SHC can be expressed as:

$$\Lambda_{\mathrm{sFD}} = \sum_{\nu_Z=0,1,2,\ldots} \Lambda_{As}(\nu_Z)\cos(\nu_Z r_{FD} Z_1 \theta_m) \tag{10}$$

where $r_{\mathrm{FD}}$ is the SHC factor. In Fig. 3, $r_{\mathrm{FD}}$ takes values such as 9/6, 11/6, 13/6, 15/6, 18/6, 17/12, 21/12, 25/12, and so forth. The stator structure also displays asymmetric configurations.

The introduction of coefficient $r_{\mathrm{FD}}$ increases the order of the rotor MMF harmonics that contribute to cogging torque (as per Inference-II), thereby reducing the overall cogging torque. This fundamental principle forms the basis of the proposed method.

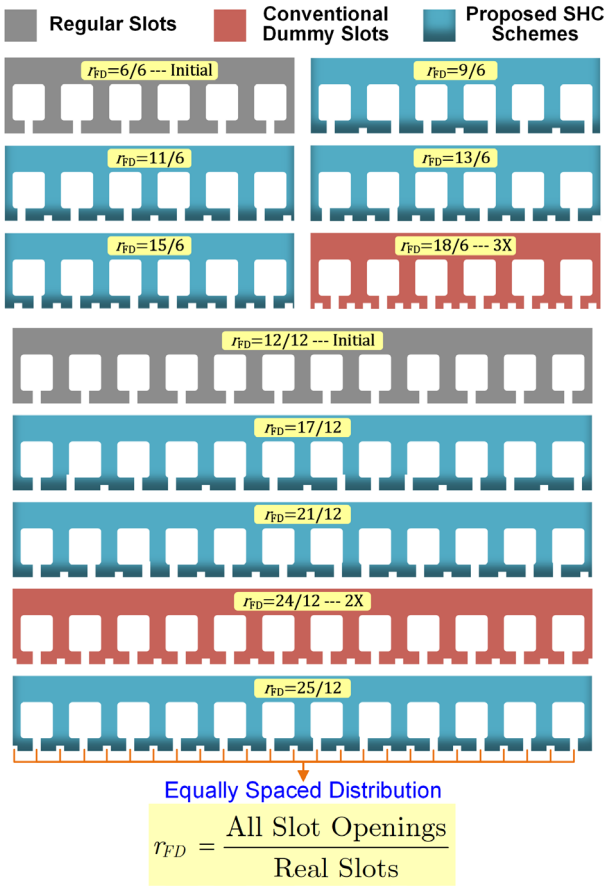


**Fig. 3.** Illustration of the proposed SHC method.

To clearly present the technical details of the proposed cogging torque reduction method, a schematic diagram illustrating the cogging torque mechanisms of regular and SHC PM machines is provided in Fig. 4. It can be observed that the introduction of the SHC coefficient enhances the LCM between the MMF and reluctance harmonics, thereby involving higher-order MMF harmonics in cogging torque generation. Since higher-order MMF harmonics generally exhibit smaller amplitudes, the suppression of cogging torque is achieved.

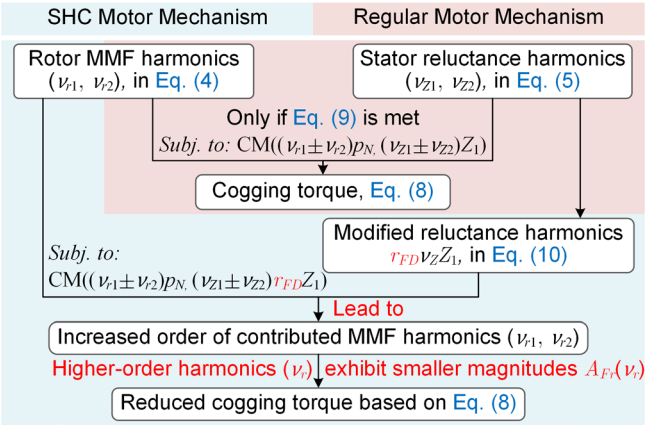


**Fig. 4.** Schematic diagram of the cogging torque mechanisms of the regular and SHC PM machines.

To compare the airgap conductance distribution before and after the implementation of SHC, the motor structure depicted in Fig. 1 underwent static FEM simulation. Initially configured as an 8-pole 24-slot motor scheme, the airgap conductance and its corresponding Fast Fourier Transform (FFT) for 12 slots are depicted in Fig. 5, revealing a symmetrical distribution within each slot. The harmonics observed align with the general description outlined in (5), where each slot encompasses harmonics such as 0, 1, 2, 3, and beyond.

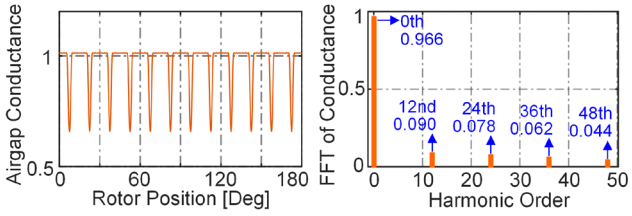


**Fig. 5.** Airgap conductance and FFT of the investigated 8-pole 24-slot PM machine. (a) Waveform. (b) FFT.

The adopted SHC with an $r_{FD}$ of 21/12 theoretically provides the 24-slot motor with the conductance characteristics of a 42-slot design, as described in (10). However, it is challenging to fully replicate the conductance characteristics of a 42-slot structure due to asymmetrical teeth, where regions with smaller tooth tip areas tend to magnetize more easily, resulting in higher magnetic conductance. Nevertheless, the SHC motor exhibits the expected high-order slot conductance harmonics.

A comparative analysis of the actual and expected airgap conductance waveforms and FFT is presented in Fig. 6. It is evident that the actual and expected distributions share similar high-order conductance components, including 21st, 42nd,

63rd, 84th, and 105th harmonics. Although the actual SHC design shows some lower-order harmonics, their contribution is minimal. The conductance harmonics are predominantly characterized by the expected higher-order harmonics, which have significant common multiples with the rotor's MMF harmonics. These LCMs are expected to mitigate the generation of severe cogging torque, as per the analysis in (8) and (9).

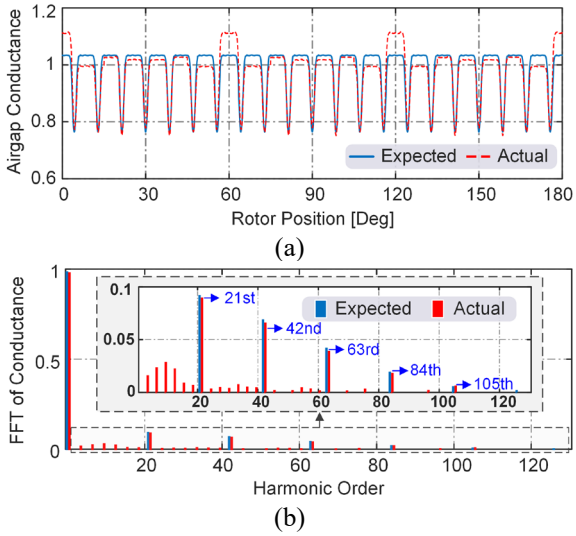


**Fig. 6.** Comparison of airgap magnetic conductance between the expected and actual $r_{FD}$ = 21/12 SHC setup. (a) Waveform comparison. (b) FFT comparison.

### *B. Recommendations for Applying the SHC Method*

For the effective implementation of the SHC method to achieve desired airgap reluctance harmonics, make the proposed method more practical, and avoid potential inter-phase imbalance generation and other undesired effects, the following design recommendations are crucial:

1) **Recommendation-1**: To ensure motor interphase balance, the SHC should be grounded on a minimum of one motor-unit, aligning the denominator of the coefficient $r_{FD}$ with the slot count per motor-unit. The total number of motor units is determined as the greatest common divisor of the slot count and pole count.
2) **Recommendation-2**: Based on the constraints imposed by the slot opening width and slot bottom width, ensure the presence of openings beneath each physical slot for easy winding insertion and to prevent core flux leakage.
3) **Recommendation-3**: Opt for smaller SHC factor to minimize the increase in effective airgap resulting from the introduction of dummy slots. This helps to prevent a reduction in flux density and torque output.

By considering these recommendations, the implementation of the SHC method can be optimized to effectively reduce cogging torque while mitigating adverse effects.

## IV. Case Studies

To validate the effectiveness and wide applicability of the proposed method, three representative PMSM structures have been chosen for the case studies: an 8-pole 24-slot surface-mounted PMSM (SPMSM), a 4-pole 24-slot interior PMSM (IPMSM), and a 10-pole 12-slot Spoke-type PMSM. Table I presents the unified structural parameters employed for these case studies, where the distinguishing factors among these cases lie in their respective rotor structures and resulting rotor MMF harmonic combinations, as well as the pole-slot matching configurations. This analysis aims to explore the applicability of different SHC schemes.

TABLE I
Unified Structural Parameters for Case Studies

| Parameter | Value | Parameter | Value |
|---|---|---|---|
| Diameter of outer stator | 200 mm | Width of slot opening | 2.5 mm |
| Diameter of inner stator | 100 mm | Height of tooth tip | 4.5 mm |
| Motor length | 90 mm | Airgap thickness | 1.5 mm |
| Winding turns | 50 | Rated current density | 2 A/mm^2 |

The electromagnetic characteristics of different SHC schemes for these three cases are simulated using the FEM. The analysis covers a comprehensive assessment of crucial electromagnetic performances, including cogging torque, back-EMF, average torque, torque ripple, and power factor.

### *A. Case I: 8p24s SPMSM*

In this case, a total of 11 design schemes are analyzed using the FEM. These include an initial design scheme with a regular stator, as well as ten SHC schemes with factors $r_{FD}$ =2, 3, 9/6, 11/6, 13/6, 15/6, 21/12, 25/12, 27/12, 29/12.

The simulations cover one electrical cycle with 180 transient points, showcasing cogging torque waveforms for different SHC schemes in Fig. 7. The initial design presents a peak cogging torque of 2.17 N·m. Multiple SHC schemes successfully mitigate cogging torque, notably the 15/6 and 21/12 configurations, which exhibit substantial reductions, resulting in peak cogging torque values of approximately 0.23 N·m and 0.19 N·m, respectively.

Furthermore, the other crucial performances of all SHC schemes are simulated and compared, performance indicators including average torque, torque ripple at rated load condition, total harmonic distortion (THD) of phase-to-phase back EMF, power factor, etc. These metrics are presented as standard index data in Table II for easy comparison. The most of SHC schemes exhibit optimized cogging torque, torque ripple (peak-peak / average), and THD of back-EMF. Although the average torque is slightly compromised due to increased effective airgap volume, this reduction remains acceptable, with a maximum deviation of 4% observed for optimal SHC schemes.

For an in-depth analysis of the optimal scheme, the $r_{FD}$ =15/6 scheme is selected for comparison with the initial design. Fig. 8 offers a comprehensive analysis of the motor structure, cogging torque, back-EMF along with its FFT, and electromagnetic torque across varying load conditions from 10% to 100%, with rated torque set at a current density of 2 A/mm². The implementation of SHC effectively suppresses cogging torque across various loads, resulting in a substantial reduction in torque ripple. Specifically, the cogging torque is suppressed by 89.5%, the torque ripple at rated load decreases from 28.6% to 10.0%, and the THD of the back-EMF is reduced from 6.77% to 5.07%.

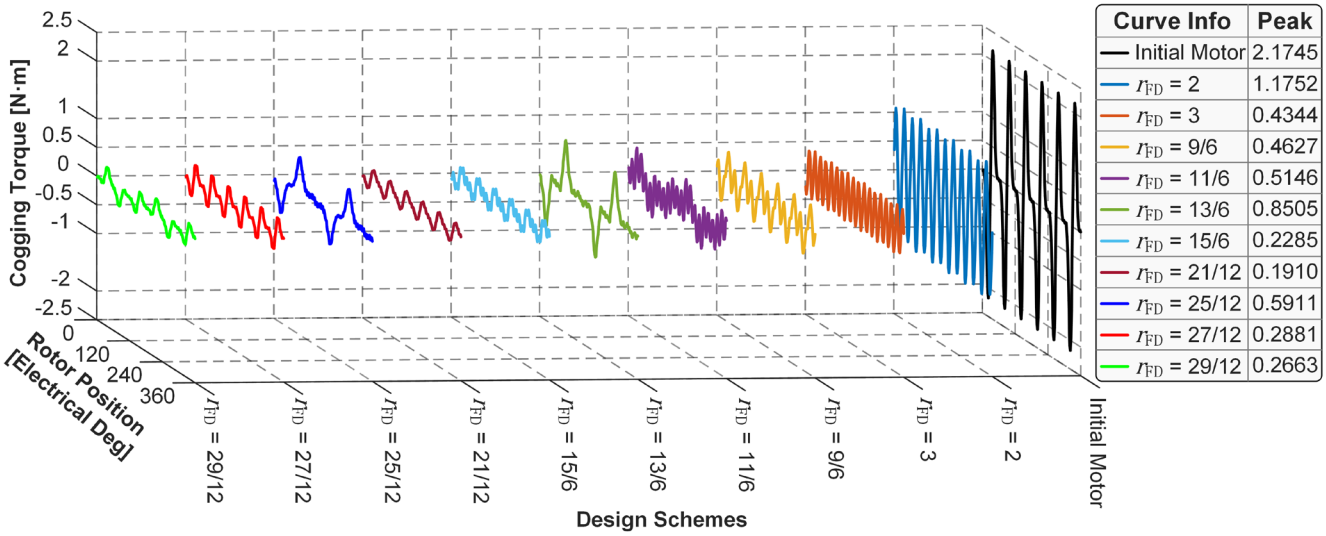


**Fig. 7.** Cogging torque waveforms of different SHC schemes of Case I.

TABLE II
COMPARISON OF COMPREHENSIVE PERFORMANCE INDICATORS OF CASE I

| Performance | Initial Motor | $r_{FD}$=2 | $r_{FD}$=3 | $r_{FD}$=9/6 | $r_{FD}$=11/6 | $r_{FD}$=13/6 | $r_{FD}$=15/6 | $r_{FD}$=21/12 | $r_{FD}$=25/12 | $r_{FD}$=27/12 | $r_{FD}$=29/12 |
|---|---|---|---|---|---|---|---|---|---|---|---|
| Peak cogging torque (p.u.) | 1 | 0.540 | 0.200 | 0.213 | 0.237 | 0.391 | 0.105 | 0.088 | 0.272 | 0.132 | 0.122 |
| Average rated torque (p.u.) | 1 | 0.995 | 0.984 | 0.954 | 0.971 | 0.975 | 0.973 | 0.966 | 0.979 | 0.972 | 0.972 |
| Torque ripple (%) | 28.6 | 20.1 | 13.9 | 9.0 | 15.0 | 20.7 | 10.0 | 5.1 | 12.5 | 7.0 | 11.7 |
| THD of phase-phase EMF (%) | 6.77 | 8.09 | 7.90 | 3.41 | 6.79 | 6.19 | 5.07 | 3.19 | 4.96 | 4.36 | 5.05 |
| Power factor | 0.9894 | 0.9891 | 0.9890 | 0.9890 | 0.9825 | 0.9900 | 0.9890 | 0.9891 | 0.9898 | 0.9890 | 0.9875 |

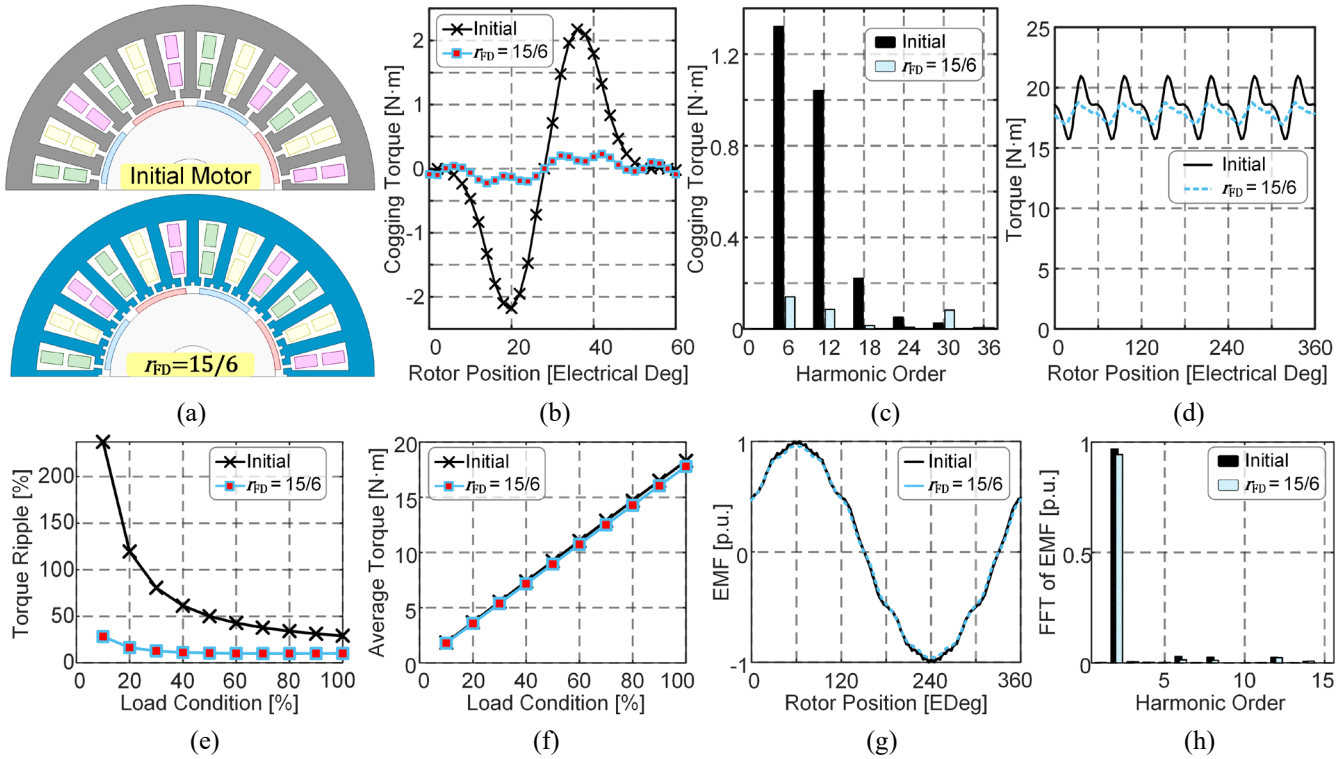


**Fig. 8.** Comprehensive analysis of Case I. (a) Motor structure comparison. (b) Cogging torque. (c) FFT of cogging torque. (d) Rated torque. (e) Torque ripple under various loads. (f) Average torque under various loads. (g) EMF. (h) FFT of EMF.

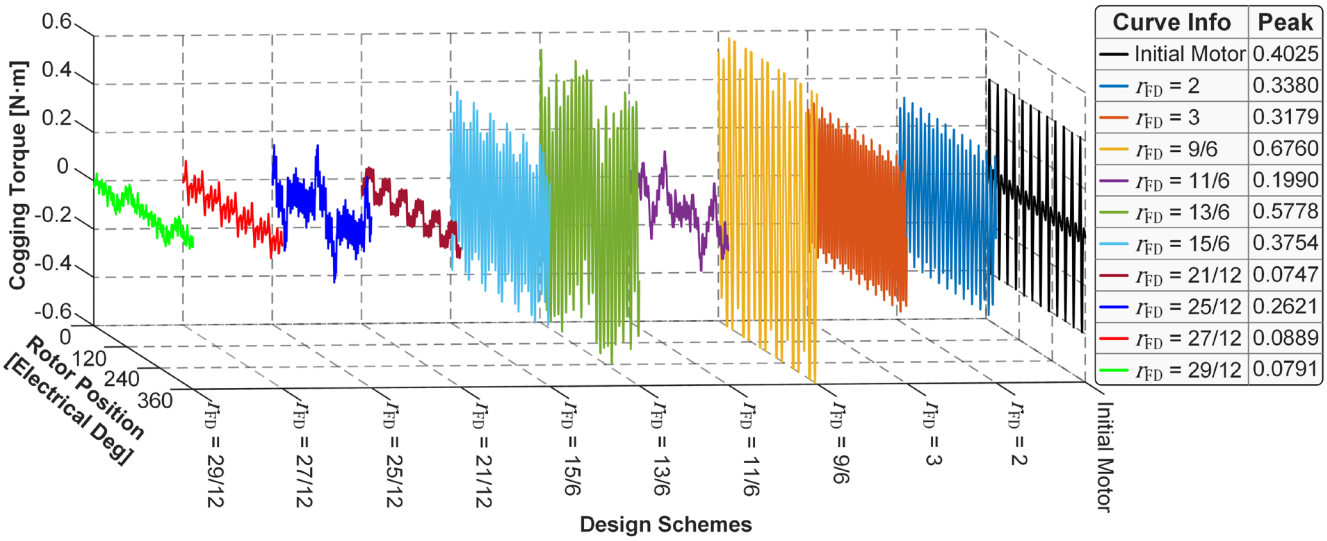


**Fig. 9.** Cogging torque waveforms of different SHC schemes of Case II.

TABLE III
COMPARISON OF COMPREHENSIVE PERFORMANCE INDICATORS OF CASE II

| Performance | Initial Motor | $r_{FD}$=2 | $r_{FD}$=3 | $r_{FD}$=9/6 | $r_{FD}$=11/6 | $r_{FD}$=13/6 | $r_{FD}$=15/6 | $r_{FD}$=21/12 | $r_{FD}$=25/12 | $r_{FD}$=27/12 | $r_{FD}$=29/12 |
|---|---|---|---|---|---|---|---|---|---|---|---|
| Peak cogging torque (p.u.) | 1 | 0.840 | 0.790 | 1.679 | 0.495 | 1.436 | 0.933 | 0.186 | 0.651 | 0.221 | 0.197 |
| Average rated torque (p.u.) | 1 | 0.993 | 0.979 | 0.991 | 0.982 | 0.982 | 0.969 | 0.966 | 0.984 | 0.980 | 0.979 |
| Torque ripple (%) | 32.13 | 29.33 | 29.47 | 41.81 | 42.08 | 52.44 | 30.22 | 15.79 | 36.71 | 28.86 | 30.83 |
| THD of phase-phase EMF (%) | 10.24 | 7.99 | 7.51 | 11.68 | 9.25 | 10.29 | 8.73 | 6.53 | 7.24 | 8.08 | 7.63 |
| Power factor | 0.9076 | 0.9045 | 0.9060 | 0.9091 | 0.8988 | 0.9102 | 0.9051 | 0.9080 | 0.9075 | 0.9080 | 0.9042 |

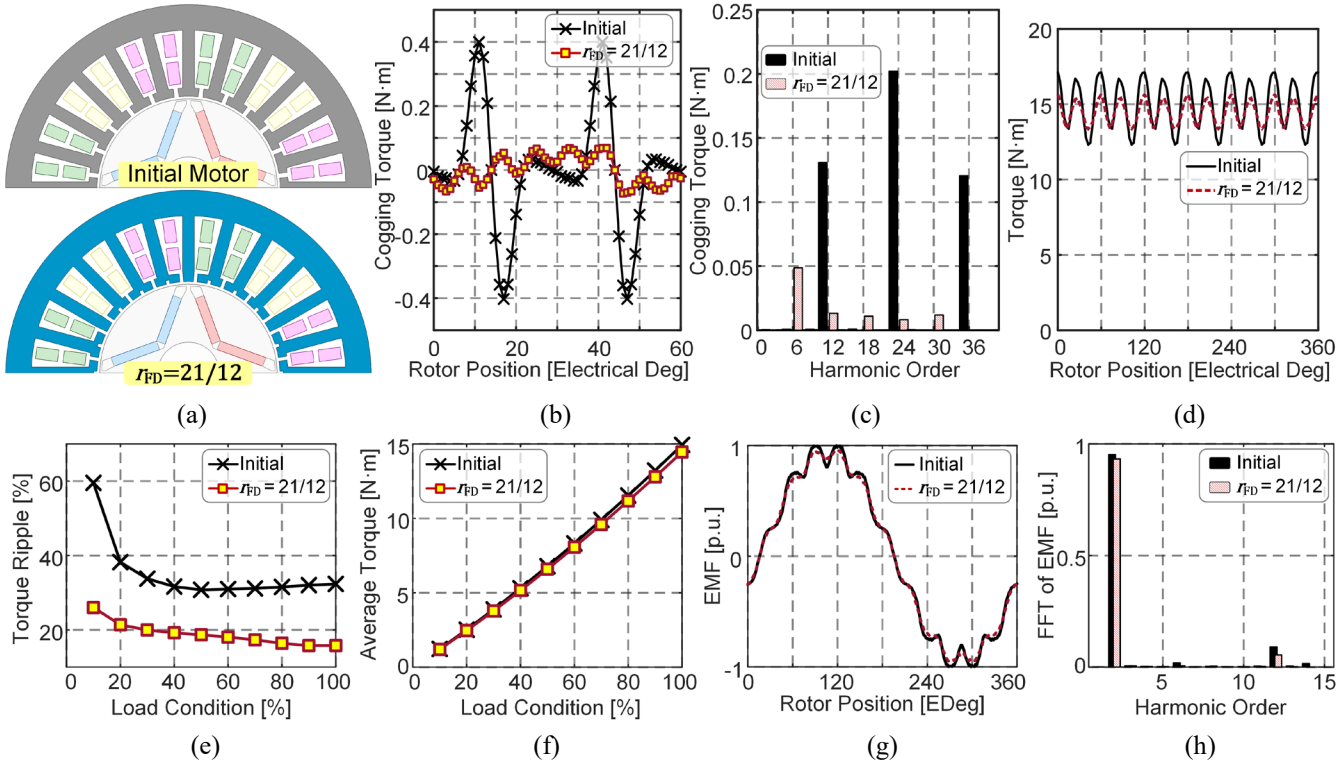


**Fig. 10.** Comprehensive analysis of Case II. (a) Motor structure comparison. (b) Cogging torque. (c) FFT of cogging torque. (d) Rated torque. (e) Torque ripple under various loads. (f) Average torque under various loads. (g) EMF. (h) FFT of EMF.

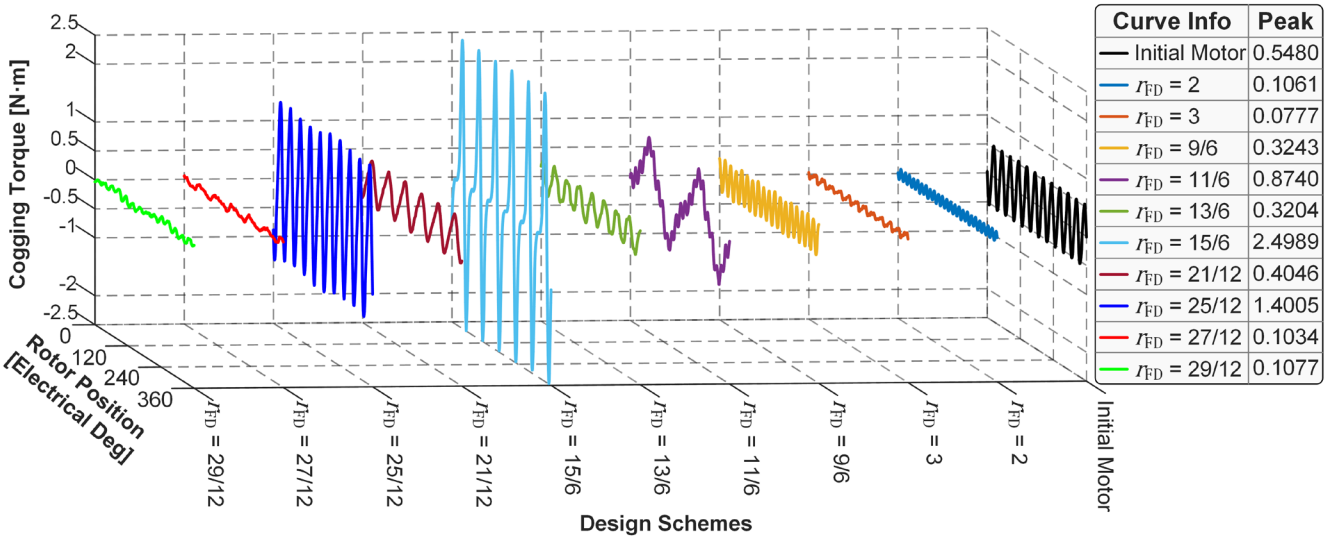


**Fig. 11.** Cogging torque waveforms of different SHC schemes of Case III.

TABLE IV
COMPARISON OF COMPREHENSIVE PERFORMANCE INDICATORS OF CASE III

| Performance | Initial Motor | $r_{FD}$=2 | $r_{FD}$=3 | $r_{FD}$=9/6 | $r_{FD}$=11/6 | $r_{FD}$=13/6 | $r_{FD}$=15/6 | $r_{FD}$=21/12 | $r_{FD}$=25/12 | $r_{FD}$=27/12 | $r_{FD}$=29/12 |
|---|---|---|---|---|---|---|---|---|---|---|---|
| Peak cogging torque (p.u.) | 1 | 0.194 | 0.142 | 0.592 | 1.595 | 0.585 | 4.560 | 0.738 | 2.556 | 0.189 | 0.197 |
| Average rated torque (p.u.) | 1 | 0.968 | 0.958 | 0.898 | 0.896 | 0.915 | 0.936 | 0.889 | 0.910 | 0.923 | 0.928 |
| Torque ripple (%) | 9.58 | 4.72 | 5.64 | 22.89 | 37.6 | 28.45 | 52.52 | 24.37 | 29.21 | 12.02 | 9.44 |
| THD of phase-phase EMF (%) | 3.41 | 3.40 | 5.09 | 12.45 | 34.82 | 13.30 | 23.94 | 10.91 | 9.95 | 8.04 | 8.75 |
| Power factor | 0.7127 | 0.7176 | 0.7704 | 0.7043 | 0.7350 | 0.7256 | 0.7498 | 0.7164 | 0.7578 | 0.7426 | 0.7600 |

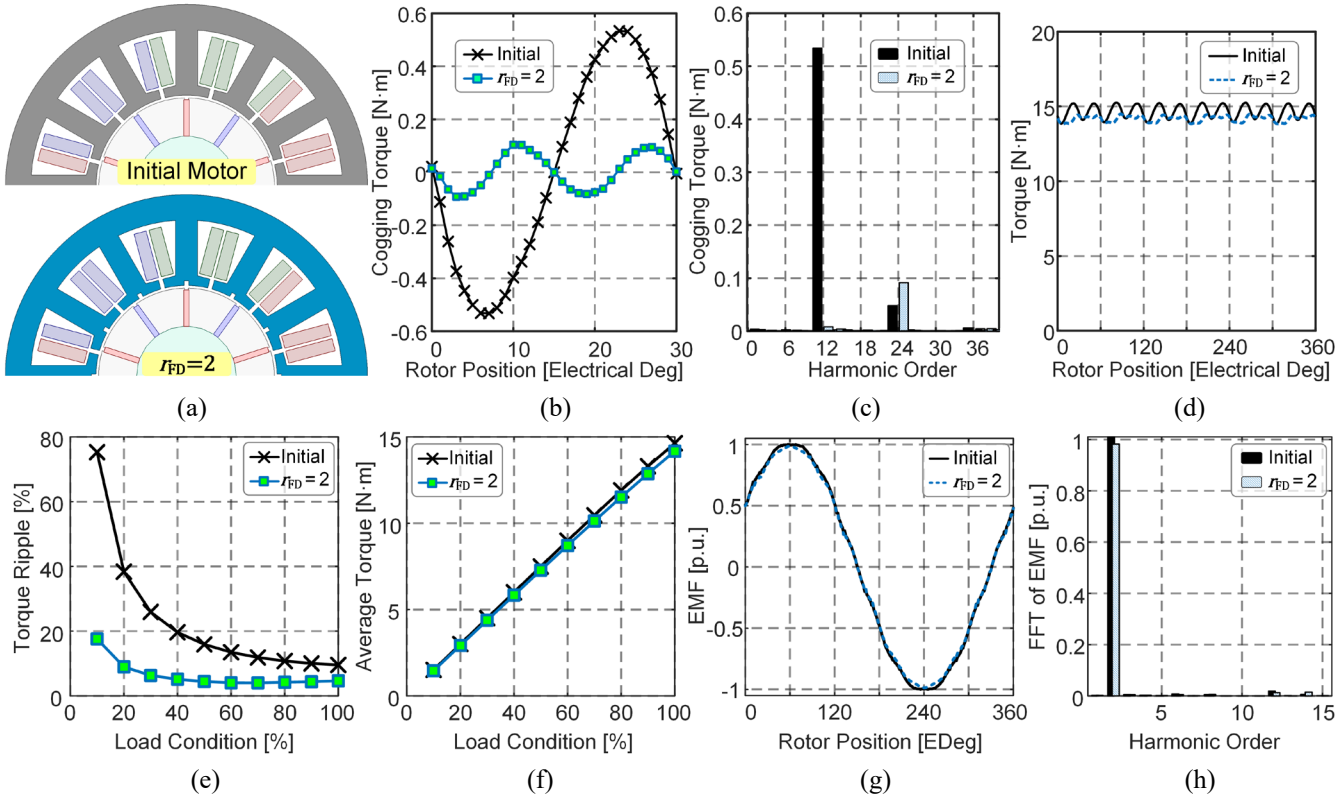


**Fig. 12.** Comprehensive analysis of Case III. (a) Motor structure comparison. (b) Cogging torque. (c) FFT of cogging torque. (d) Rated torque. (e) Torque ripple under various loads. (f) Average torque under various loads. (g) EMF. (h) FFT of EMF.

### B. Case II: 4p24s IPMSM

The pole-slot factor investigated is commonly employed in electric vehicles. In this study, simulations of 11 SHC schemes were conducted over a single electrical cycle using 360 points to analyze their cogging torque waveforms, as shown in Fig. 9.

In the case of this distributed-winding motor, the cogging torque primarily stems from the 11th and 13th harmonics of the rotor MMF. Hence, the cogging torque is not significant, with the initial design showing a peak cogging torque of approximately 0.403 N·m. Further reduction in cogging torque is achievable through the application of the SHC method. Fig. 9 indicates that the cogging torque is significantly decreased to 0.075 N·m in the $r_{\mathrm{FD}}$ =21/12 SHC scheme.

Table III provides a comparison of various performance metrics across all SHC schemes. The data indicate that the 21/12 SHC scheme delivers superior performance, with an 81.4% decrease in cogging torque, a reduction in torque ripple from 32.1% to 15.8%, and a suppression of the THD of the back-EMF from 10.24% to 6.53%. The average torque experiences only a minor 3.4% compromise.

These findings highlight the effectiveness of the 21/12 SHC scheme in improving various performance aspects. For a detailed comparison with the initial design, the 21/12 scheme was selected. Fig. 10 showcases the motor structures, cogging torques, torques under different load conditions, and back-EMFs for both motors, highlighting notable reductions in cogging torque and torque ripples under varied conditions.

### C. Case III: 10p12s IPMSM

The 10-pole 12-slot PMSM configuration is widely acknowledged for its superior performance, characterized by minimal cogging torque, torque ripple, and back-EMF distortion. Initially, this design displays a cogging torque of around 0.548 N·m, which is further reduced through the implementation of SHC methods, as illustrated in Fig. 11.

In this fractional-slot combination, employing SHC with a denominator of 6 might introduce lower-order slot harmonics, potentially elevating cogging torque. Additionally, employing SHC with a denominator of 12 could reduce cogging torque but might inadvertently induce back-EMF distortion.

Nevertheless, utilizing SHC with an integer $r_{\mathrm{FD}}$ proves to be a more promising strategy for mitigating cogging torque and improving overall motor performances. In this context, the $r_{\mathrm{FD}} = 2$ and $r_{\mathrm{FD}} = 3$ SHCs effectively reduce the cogging torque from 0.548 N·m to 0.106 N·m and 0.078 N·m, respectively. A comprehensive analysis of the performance indicators for all SHC schemes is provided in Table IV.

The $r_{\mathrm{FD}} = 2$ SHC is chosen for detailed comparison with the initial design, as the $r_{\mathrm{FD}} = 3$ SHC results in a more pronounced decrease in average torque, and the comparison is shown in Fig. 12. Upon comparison, various performance aspects are enhanced through integral SHC design. For the $r_{\mathrm{FD}} = 2$ scheme, cogging torque sees an 80.6% reduction, while the torque ripple under rated load conditions decreases from 9.58% to 4.72%. Consequently, the SHC with an integer $r_{\mathrm{FD}}$ is better suited for fractional-slot motors.

Under different pole-slot combinations, the proposed SHC designs can optimize cogging torque and other performances to varying degrees, validating the effectiveness and wide applicability of the proposed method.

Furthermore, with a uniform pole-slot combination, the SHC designs for cogging torque suppression theoretically extends to various rotor structures. This is because SHC directly adjusts the rotor MMF harmonic orders that lead to cogging torque, providing a more effective solution to structural modifications.

### D. Discussion on Selecting the Optimal SHC Scheme

The analyses of the three cases demonstrate that different SHC schemes have varying performance impacts on motor structures with different slot-pole combinations. Some SHC designs significantly enhance performance, while others may degrade torque and electromagnetic characteristics, making a summary discussion necessary.

1. Integer-slot PM machines:

For integral slot PM machines, it is more suitable to adopt SHC factors that are fractional. This approach theoretically increases the LCM between the rotor MMF harmonic and the airgap reluctance harmonic, effectively suppressing cogging torque. However, it is important to note that some fractional SHC factors may inadvertently increase cogging torque. This occurs because the SHC generates higher-order reluctance harmonics while also introducing some lower-order harmonics, as analyzed in Section III.A. These lower-order harmonics may interact with the rotor MMF harmonics, potentially resulting in increased cogging torque.

Overall, whether for concentrated or distributed windings, an $r_{\mathrm{FD}} = 21/12$ is a recommended solution, as it does not significantly increase the number of slot openings, thereby avoiding torque losses, and both integral slot cases demonstrate excellent performance improvement.

2. Fractional-slot PM machines:

Fractional slot machines typically exhibit minimal cogging torque due to the large LCM of their pole and slot numbers. To further suppress cogging torque, using an integer SHC factor can achieve rapid, effective, and reliable cogging torque reduction and enhancement of electromagnetic performance.

In this context, $r_{\mathrm{FD}} = 2$ stands out as a recommended scheme, as it provides noticeable performance improvements with minimal torque sacrifice.

Lastly, it is worth noting that cogging torque, when suppressed using SHC method, may be further diminished by carefully considering and optimizing key structural parameters, such as slot opening width, opening depth, rotor MMF harmonic distribution, among others.

## V. Experimental Validation

In order to experimentally validate the efficacy of the proposed method in suppressing cogging torque and enhancing overall performance, the SHC scheme with the factor $r_{\mathrm{FD}}$ =21/12 is selected for the stator reconstruction of a 4-pole, 24-slot motor with Delta-type IPMs.

### A. Comparative Prototypes and Testing Platform

Comparative prototypes of the initial and optimal SHC

designs are fabricated for intuitive comparison. The stator and rotor laminations are shown in Fig. 13, clearly illustrating their shared rotor structure. However, notable differences exist in the stator tooth. The SHC design features 21 slot openings per 12 actual slots.

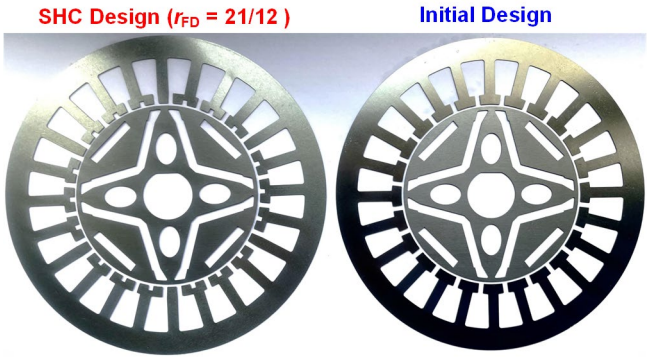


**Fig. 13.** Motor laminations. (a) SHC design. (b) Initial design.

The fabricated motors and testing platforms are shown in Fig. 14. Cogging torque testing is conducted using a balancing weight measurement platform. The stator is securely fixed, and its position is adjusted using an indexing dial, while the rotor is connected to a balancing bar to ensure equilibrium. As the indexing dial rotates gradually, the weight of the masses is recorded and converted to calculate the cogging torque. Furthermore, the torque ripple is tested using a load testing platform equipped with a brake and a torque transducer.

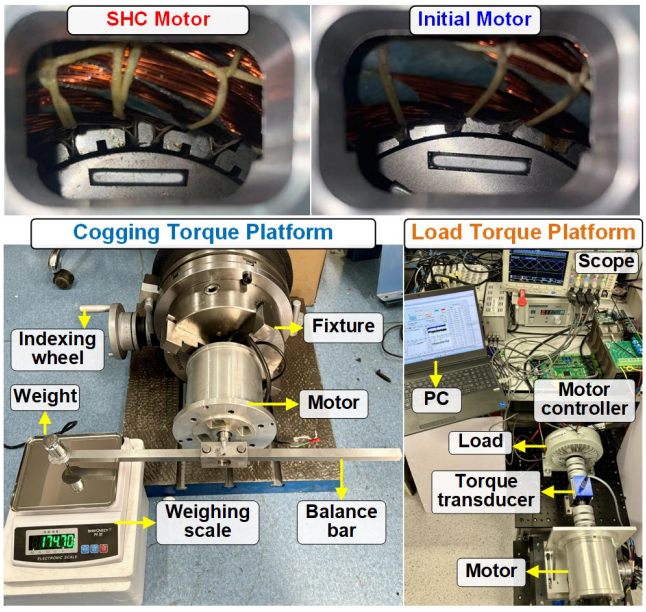


**Fig. 14.** Motor prototypes and testing platforms.

*B. No-load Performance*

The cogging torques of the two motors were simulated and tested, with their waveforms and FFT analysis results are presented in Fig. 15. The peak cogging torque values obtained from the FEM simulations are 181 mN·m and 84.5 mN·m, while the corresponding values from the tests are approximately 191 mN·m and 65.9 mN·m.

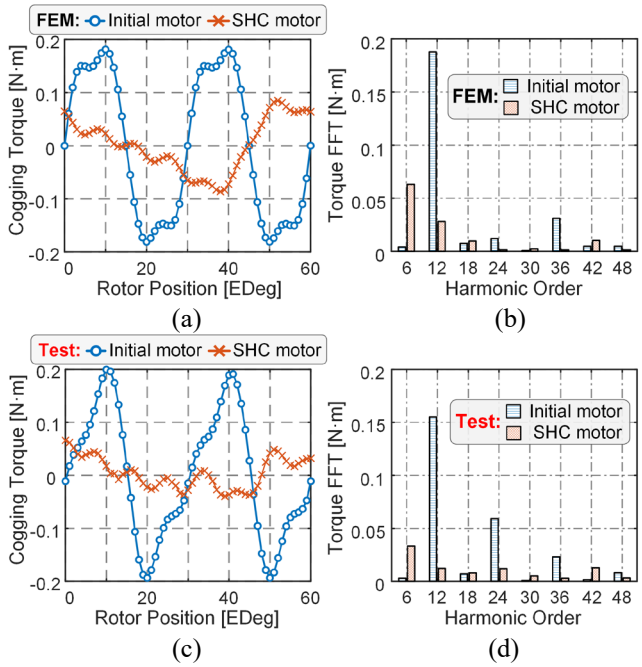


**Fig. 15.** Comparison of cogging torque between the two motors. (a) Simulated cogging torque. (b) FFT of simulated cogging torque. (c) Tested cogging torque. (d) FFT of tested cogging torque.

Upon comparing the FFT results, the order and distribution patterns of cogging torque between simulation and experiment appear similar, with the initial motor predominantly exhibiting the 12th order and the SHC motor primarily showcasing the 6th order. However, in contrast between simulation and experiment, differences in the magnitude of each order exist. These variations may stem from: 1) manufacturing tolerances and assembly errors; 2) inaccurate simulation of the specific values of chamfering on the edges of PMs and coating thickness; 3) variations in the performance of the PMs, differences in residual magnetism among different magnets, and the possibility of uneven magnetization in a single magnet.

Nevertheless, overall, the SHC design demonstrates a notable effectiveness in suppressing cogging torque, both in experiment and simulation.

Moreover, the phase-to-phase back-EMF of the two motors were simulated and tested, with their waveforms and FFT analysis results shown in Fig. 16. The FFT results reveal that at the same speed, the fundamental component of the back EMFs of the initial motor and the SHC motor differ by approximately 1V, indicating a torque loss of around 2% with the SHC implementation. Additionally, while the distribution of harmonics shows similarities between the experiment and simulation, the experimental data exhibit a more pronounced degree of harmonic distortion, likely for reasons similar to those previously mentioned. Overall, the SHC design demonstrates a notable improvement in reducing back EMF harmonic distortion, as supported by both sets of results.

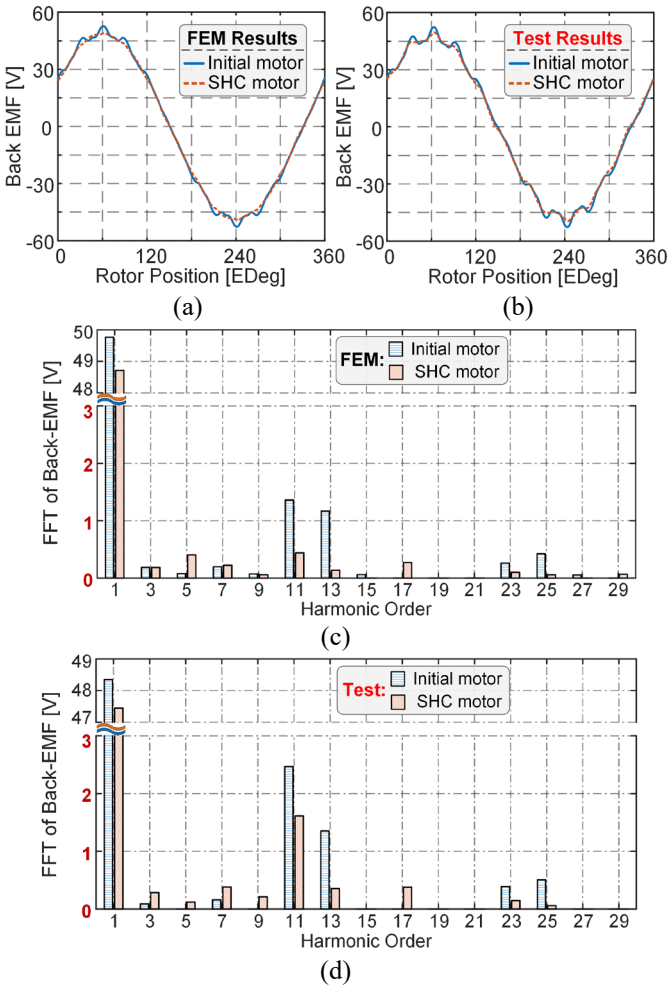


**Fig. 16.** Comparison of phase-to-phase back-EMF between the two motors. (a) Simulated back-EMF. (b) Tested back-EMF. (c) FFT of simulated back-EMF. (d) FFT of tested back-EMF.

### *C. On-load Performance*

The torque and three-phase currents of the two motors under different load conditions were tested, and their waveform comparison is shown in Fig. 17. The motors were operated at 120 rpm under speed closed-loop control. The load torque was applied using a magnetic powder brake, renowned for its stable load torque provision. Dynamic torque was measured using a high-dynamic torque transducer, and the torque signal was recorded by an oscilloscope.

Both motors exhibited minimal current distortion when operating under the same controller and control parameters. The torque comparison revealed that the SHC motor exhibited smaller torque ripples.

Furthermore, both motors demonstrated nearly identical torque outputs per unit current, indicating that the SHC method effectively suppresses torque ripple without compromising the torque density.

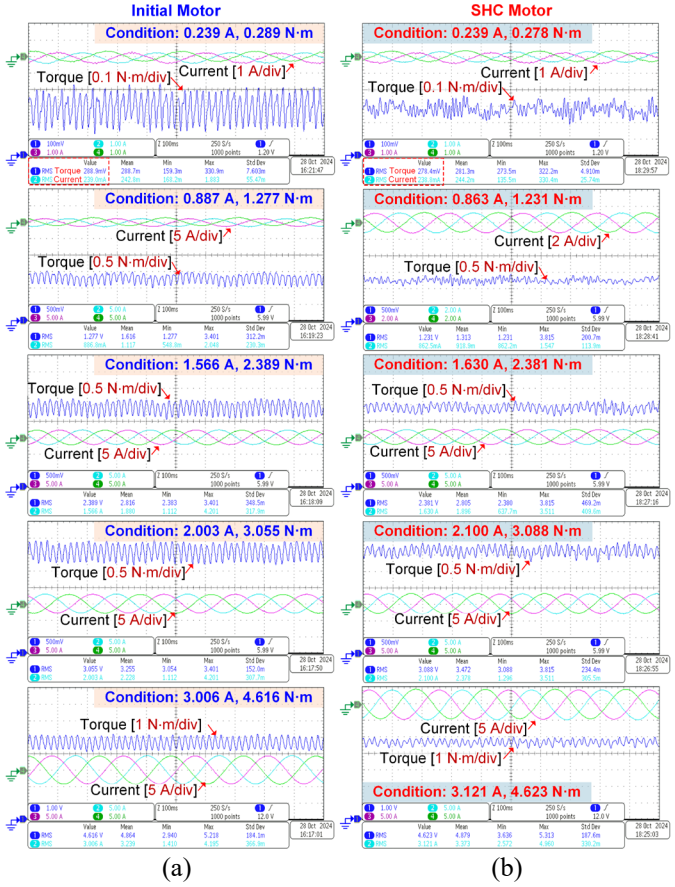


**Fig. 17.** Torque and current waveforms under various load conditions. (a) Initial motor. (b) SHC motor.

## VI. Conclusion

This paper proposes a generalized SHC method coupled with diverse slot-opening design schemes to reduce cogging torque in PM machines. The method introduces the coefficient $r_{FD}$ to enable the implementation of various SHCs. The effectiveness of this approach has been validated through extensive simulation cases and experimental validations, demonstrating its capability to not only reduce cogging torque but also improve back-EMF harmonic distortion and torque ripple. Therefore, this study introduces a novel optimization path for motor designers.

From the comprehensive analysis conducted, the following conclusions are drawn:

1) Integer-slot machines are more suitable for adopting fractional SHC factors, while conversely, fractional-slot machines are better suited for using integer SHC factors.
2) The potential generation of low-order harmonics by SHCs is a topic worthy of further exploration. This includes understanding the generation patterns of low-order reluctance harmonics in relation to SHC factors and optimizing structural parameters to prevent low-order harmonics from adversely affecting torque and electromagnetic performance. Optimizable parameters may include slot opening width, the initial angle of the overall slot opening, and the design of non-uniform slot openings.

3) Further exploration of additional forms of SHC factors is anticipated. Although this paper aims to explore various SHC schemes, the scope remains limited. Some schemes were not analyzed due to the design constraint of having narrow openings beneath the slots, which complicates winding insertion. However, considering the overall offset of the slot openings may resolve this issue. Additionally, cases where the numerator of the SHC factor is even have not been discussed and also warrant further analysis.

## REFERENCES


[1] Y. Yang et al., "Design and Comparison of Interior Permanent Magnet Motor Topologies for Traction Applications," *IEEE Trans. Transport. Electrific.*, vol. 3, no. 1, pp. 86-97, March 2017.

[2] B. Sarlioglu and C. T. Morris, "More Electric Aircraft: Review, Challenges, and Opportunities for Commercial Transport Aircraft," *IEEE Trans. Transport. Electrific.*, vol. 1, no. 1, pp. 54-64, June 2015.

[3] H. M. Flieh, R. D. Lorenz, E. Totoki, S. Yamaguchi and Y. Nakamura, "Investigation of Different Servo Motor Designs for Servo Cycle Operations and Loss Minimizing Control Performance," *IEEE Trans. Ind. Appl.*, vol. 54, no. 6, pp. 5791-5801, Nov.-Dec. 2018.

[4] M. Degano et al., "Optimised Design of Permanent Magnet Assisted Synchronous Reluctance Machines for Household Appliances," *IEEE Trans. Energy Convers.*, vol. 36, no. 4, pp. 3084-3095, Dec. 2021.

[5] Z. Q. Zhu, L. J. Wu and Z. P. Xia, "An Accurate Subdomain Model for Magnetic Field Computation in Slotted Surface-Mounted Permanent-Magnet Machines," *IEEE Trans. Magn.*, vol. 46, no. 4, pp. 1100-1115, April 2010.

[6] N. Bianchi and S. Bolognani, "Design techniques for reducing the cogging torque in surface-mounted PM motors," *IEEE Trans. Ind. Appl.*, vol. 38, no. 5, pp. 1259-1265, Sept.-Oct. 2002.

[7] R. Islam, I. Husain, A. Fardoun and K. McLaughlin, "Permanent-Magnet Synchronous Motor Magnet Designs With Skewing for Torque Ripple and Cogging Torque Reduction," *IEEE Trans. Ind. Appl.*, vol. 45, no. 1, pp. 152-160, Jan.-Feb. 2009.

[8] Z. S. Du and T. A. Lipo, "Reducing Torque Ripple Using Axial Pole Shaping in Interior Permanent Magnet Machines," *IEEE Trans. Ind. Appl.*, vol. 56, no. 1, pp. 148-157, Jan.-Feb. 2020.

[9] D. Wang, C. Peng, J. Li and C. Wang, "Comparison and Experimental Verification of Different Approaches to Suppress Torque Ripple and Vibrations of Interior Permanent Magnet Synchronous Motor for EV," *IEEE Trans. Ind. Electron.*, vol. 70, no. 3, pp. 2209-2220, March 2023.

[10] L. Dai, S. Niu, W. Zhang, J. Gao and S. Huang, "Harmonic Modeling and Ripple Suppression of Electromagnetic Torque in IPMSMs," *IEEE Trans. Ind. Electron.*, vol. 71, no. 12, pp. 16223-16233, Dec. 2024.

[11] L. Dai, J. Gao, S. Niu, K. Liu, S. Huang and W. L. Chan, "Cogging Torque Suppression for IPMSM Based on Flux Harmonic Configuration," *IEEE Trans. Ind. Electron.*, Early Access, doi: 10.1109/TIE.2024.3443959.

[12] V. Simón-Sempere, A. Simón-Gómez, M. Burgos-Payán and J. -R. Cerquides-Bueno, "Optimisation of Magnet Shape for Cogging Torque Reduction in Axial-Flux Permanent-Magnet Motors," *IEEE Trans. Energy Convers.*, vol. 36, no. 4, pp. 2825-2838, Dec. 2021.

[13] O. O. Ogidi, P. S. Barendse and M. A. Khan, "Influence of Rotor Topologies and Cogging Torque Minimization Techniques in the Detection of Static Eccentricities in Axial-Flux Permanent-Magnet Machine," *IEEE Trans. Ind. Appl.*, vol. 53, no. 1, pp. 161-170, Jan.-Feb. 2017.

[14] S. S. R. Bonthu, M. T. B. Tarek and S. Choi, "Optimal Torque Ripple Reduction Technique for Outer Rotor Permanent Magnet Synchronous Reluctance Motors," *IEEE Trans. Energy Convers.*, vol. 33, no. 3, pp. 1184-1192, Sept. 2018.

[15] J. Qi et al., "Suppression of Torque Ripple for Consequent Pole PM Machine by Asymmetric Pole Shaping Method," *IEEE Trans. Ind. Appl.*, vol. 58, no. 3, pp. 3545-3557, May-June 2022.

[16] C. Gan, J. Wu, M. Shen, W. Kong, Y. Hu and W. Cao, "Investigation of Short Permanent Magnet and Stator Flux Bridge Effects on Cogging Torque Mitigation in FSPM Machines," *IEEE Trans. Energy Convers.*, vol. 33, no. 2, pp. 845-855, June 2018.

[17] C. Chen, X. Ren, D. Li, R. Qu, K. Liu and T. Zou, "Torque Performance Enhancement of Flux-Switching Permanent Magnet Machines With Dual Sets of Magnet Arrangements," *IEEE Trans. Transport. Electrific.*, vol. 7, no. 4, pp. 2623-2634, Dec. 2021.

[18] Q. Lin, S. Niu and W. N. Fu, "Design and Optimization of a Dual-Permanent-Magnet Vernier Machine With a Novel Optimization Model," *IEEE Trans. Magn.*, vol. 56, no. 3, pp. 1-5, March 2020, Art no. 7512705.

[19] J. Wanjiku, M. A. Khan, P. S. Barendse and P. Pillay, "Influence of Slot Openings and Tooth Profile on Cogging Torque in Axial-Flux PM Machines," *IEEE Trans. Ind. Electron.*, vol. 62, no. 12, pp. 7578-7589, Dec. 2015.

[20] S. Leitner, H. Gruebler and A. Muetze, "Cogging Torque Minimization and Performance of the Sub-Fractional HP BLDC Claw-Pole Motor," *IEEE Trans. Ind. Appl.*, vol. 55, no. 5, pp. 4653-4664, Sept.-Oct. 2019.

[21] Z. Zhang, P. Wang, W. Hua, T. Zhang, G. Wang and M. Hu, "Comprehensive Investigation and Evaluation of Cogging Torque Suppression Techniques of Flux-Switching Permanent Magnet Machines," *IEEE Trans. Transport. Electrific.*, vol. 9, no. 3, pp. 3894-3907, Sept. 2023.

[22] J. H. Kim, Y. Li, E. Cetin and B. Sarlioglu, "Influence of Rotor Tooth Shaping on Cogging Torque of Axial Flux-Switching Permanent Magnet Machine," *IEEE Trans. Ind. Appl.*, vol. 55, no. 2, pp. 1290-1298, March-April 2019.

[23] Q. Li, J. Yang, Y. Pan, S. Dai, Y. Feng and S. Huang, "Investigation and Suppression of Cogging Torque of Permanent Magnet Homopolar Inductor Machine," *IEEE Trans. Ind. Electron.*, vol. 71, no. 3, pp. 2253-2264, March 2024.

[24] M. Nakano, Y. Morita and T. Matsunaga, "Reduction of Cogging Torque Due to Production Tolerances of Rotor by Using Dummy Slots Placed Partially in Axial Direction," *IEEE Trans. Ind. Appl.*, vol. 51, no. 6, pp. 4372-4382, Nov.-Dec. 2015.

[25] Y. -U. Park, J. -H. Cho and D. -k. Kim, "Cogging Torque Reduction of Single-Phase Brushless DC Motor With a Tapered Air-Gap Using Optimizing Notch Size and Position," *IEEE Trans. Ind. Appl.*, vol. 51, no. 6, pp. 4455-4463, Nov.-Dec. 2015.

[26] Y. Yokoi and T. Higuchi, "Stator Design of Alternate Slot Winding for Reducing Torque Pulsation With Magnet Designs in Surface-Mounted Permanent Magnet Motors," *IEEE Trans. Magn.*, vol. 51, no. 6, pp. 1-11, June 2015.

[27] G. Zhao, W. Hua, X. Zhu and G. Zhang, "The Influence of Dummy Slots on Stator Surface-Mounted Permanent Magnet Machines," *IEEE Trans. Magn.*, vol. 53, no. 6, pp. 1-5, June 2017.

[28] L. Dai, J. Gao, S. Niu and S. Huang, "Multi-Electromagnetic Performance Optimization of Double-Layer Interior Permanent Magnet Synchronous Machine," *IEEE Trans. Ind. Electron.*, vol. 71, no. 11, pp. 14535-14545, Nov. 2024.

[29] D. Wang, C. Peng, B. Wang, Z. Feng and J. Li, "Permanent Magnet Synchronous Machines With Nonuniformly Distributed Teeth," *IEEE Trans. Ind. Electron.*, vol. 69, no. 9, pp. 8705-8715, Sept. 2022.

[30] T. Liu, S. Huang, J. Gao and K. Lu, "Cogging Torque Reduction by Slot-Opening Shift for Permanent Magnet Machines," *IEEE Trans. Magn.*, vol. 49, no. 7, pp. 4028-4031, July 2013.

[31] Z. Q. Zhu, S. Ruangsinchaiwanich, D. Ishak and D. Howe, "Analysis of cogging torque in brushless Machines having nonuniformly distributed stator slots and stepped rotor magnets," *IEEE Trans. Magn.*, vol. 41, no. 10, pp. 3910-3912, Oct. 2005.

[32] L. J. Wu, Z. Q. Zhu, D. Staton, M. Popescu and D. Hawkins, "Analytical cogging torque prediction for surface-mounted PM machines accounting for different slot sizes and uneven positions," 2011 IEEE International Electric Machines & Drives Conference (IEMDC), Niagara Falls, ON, Canada, 2011, pp. 1322-1327.

[33] R. P. Deodhar, D. A. Staton, T. M. Jahns and T. J. E. Miller, "Prediction of cogging torque using the flux-MMF diagram technique," *IEEE Trans. Ind. Appl.*, vol. 32, no. 3, pp. 569-576, May-June 1996.



**Litao Dai** (Member, IEEE) was born in Changsha, China, in 1993. He received the B.S. degree in mathematics from Harbin University of Commerce, Harbin, China, in 2015, and Ph.D. degree in electrical engineering from Hunan University, Changsha, China, in 2023.

He is currently working as a Postdoctoral Fellow with the Department of Electrical and Electronic Engineering, The Hong Kong Polytechnic University, Hong Kong, SAR, China.

**Shuangxia Niu** (Senior Member, IEEE) received the B.Sc. and M.Sc. degrees from Tianjin University, Tianjin, China, in 2002 and 2005, and the Ph.D. degree from the University of Hong Kong, Hong Kong, SAR, China, in 2009, all in electrical engineering.

She is currently a professor with the Department of Electrical and Electronic Engineering, The Hong Kong Polytechnic University. She authored or coauthored more than 200 papers in leading journals. Prof. Niu is currently an Associate Editor of the IEEE Transactions on Industrial Electronics and an Associate Editor for the IEEE Journal of Emerging and Selected Topics in Power Electronics.

**Jian Gao** received his B.E., M.E., and Ph.D. degrees in electrical engineering from Hunan University, Changsha, China, in 2001, 2004, and 2013, respectively.

From 2004 to 2021, he served as a Lecture and Associate Professor with the College of Electrical and Information Engineering, Hunan University, where he now served as a Full Professor. His research interests include high power/torque density motor design and control, wind energy conversion systems, and vehicle electric drive systems.

**Kun Liu** was born in China, in 1998. He received the B.S. degree in electrical engineering from Anhui University of Science and Technology, Anhui, China, in 2020, and the M.E. degree in electrical engineering from Hunan University, Hunan, China, in 2023.

He is currently working as a research assistant with the College of Electrical and Information Engineering, Hunan University, Hunan, China.

**Shoudao Huang** (Senior Member, IEEE) received the B.S. and Ph.D. degrees in electrical engineering from Hunan University, Changsha, China, in 1983, and 2005, respectively.

He is currently a Full Professor with the College of Electrical and Information Engineering, Hunan University, China. His research interests include wind energy conversion system, generator design and control, and electronic system and control.

**W. L. Chan** (Senior Member, IEEE) received the B.Sc.(Eng.) and M.Phil. degrees from The University of Hong Kong, Hong Kong, in 1988 and 1993. He then received Ph.D. degree from City University London, London, U.K, in 2000.

He is now an Associate Professor in the Department of Electrical and Electronic Engineering, The Hong Kong Polytechnic University. Dr. Chan is the Vice Chairman of the International Association of Elevator Engineers (Hong Kong-China Branch).